Int J Adv Manuf Technol (2014) 74:1691–1699
DOI 10.1007/s00170-014-6099-6

ORIGINAL ARTICLE

Micromachining of stainless steel–polymer composites using nanosecond and femtosecond UV lasers

Daehwan Ahn · Changho Seo · Taesoon Park · Dongyong Park · Seongjin Park · Youngsam Kwon · Dongsik Kim

Received: 13 September 2012 / Accepted: 24 June 2014 / Published online: 8 July 2014

Abstract The fabrication of microstructures using high-strength anti-corrosive materials is a topic of intense investigation. In this work, we investigate micromachining processes for fabricating stainless steel–polymer composites using nanosecond (excimer) and femtosecond (Ti:sapphire) lasers at ultraviolet wavelengths. The laser ablation mechanisms were analyzed as a function of the laser source and process parameters. Microdrilling and grooving of the composite were used to evaluate the process performance. The ns laser processing mechanism at relatively low fluences relied mainly on ablation with photothermal/photochemical decomposition of the binder resin without permanently affecting the stainless steel particles. On the other hand, ns laser pulse irradiation at high fluences induced significant melting and agglomeration of the particles, which lowered the ablation rate and were detrimental to the micromachining performance. During the high-intensity femtosecond laser processing (>TW/cm^2), the laser pulse directly ablated the particles and the binder without inducing significant thermal effects. Microstructures 10 μm in size (average particle size) and with an aspect ratio of ~10 were fabricated.

Keywords Excimer laser · Laser micromachining · Powder composite · Stainless steel · Stainless steel–polymer composite · Ti:sapphire laser

D. Ahn · C. Seo · T. Park · D. Park · S. Park · D. Kim (✉)
Department of Mechanical Engineering, POSTECH,
Pohang 790-784, Republic of Korea
e-mail: dskim87@postech.ac.kr

Y. Kwon
CetaTech Co. Ltd, Sacheon 664-953, Republic of Korea

1 Introduction

Technologies for producing three-dimensional microscale components using high-strength anti-corrosive materials, such as tungsten carbide, alumina, and stainless steel, are important in a variety of applications, including microfluidics, micromechanics, biosensors, and microelectronic packaging [1–4]. Micro powder injection molding (μ-PIM), which combines powder injection molding (PIM) with microinjection molding techniques, was developed to fabricate microscale components for these applications [5–7]; however, μ-PIM is limited in its ability to produce components with a desired microstructure because the quality of injection, which is largely determined by the rheological characteristics of the powder system, is governed by multiple parameters, including the binder composition [8], binder/powder ratio [9], and injection parameters [10, 11], that are related in a complex manner. Accordingly, several studies have pursued optimal conditions for filling molds with small particles without forming cavities. These studies examined ranges of parameters, such as the binder system design, feedstock, part geometry, mold design, and processing conditions [12–15]. Recently, the μ-PIM technique was used to produce microstructures using a stainless steel–polymer composite (316 L, D_{50}=4.5 μm) with a feature size of 20 μm [16].

An alternative approach to fabricating microstructures using high-strength anti-corrosive materials involves laser micromachining of a stainless steel–polymer composite comprising a powder composite held together by a binder resin. For example, laser beams can be used to produce microstructures on injection-molded parts prior to sintering. The powder composite is formed using a polymer binder, and a laser beam can easily break the polymer bonds in the binder to selectively remove the polymer binder, producing a microstructured powder composite (Fig. 1). Several studies were conducted to develop laser-based micromachining processes for the powder

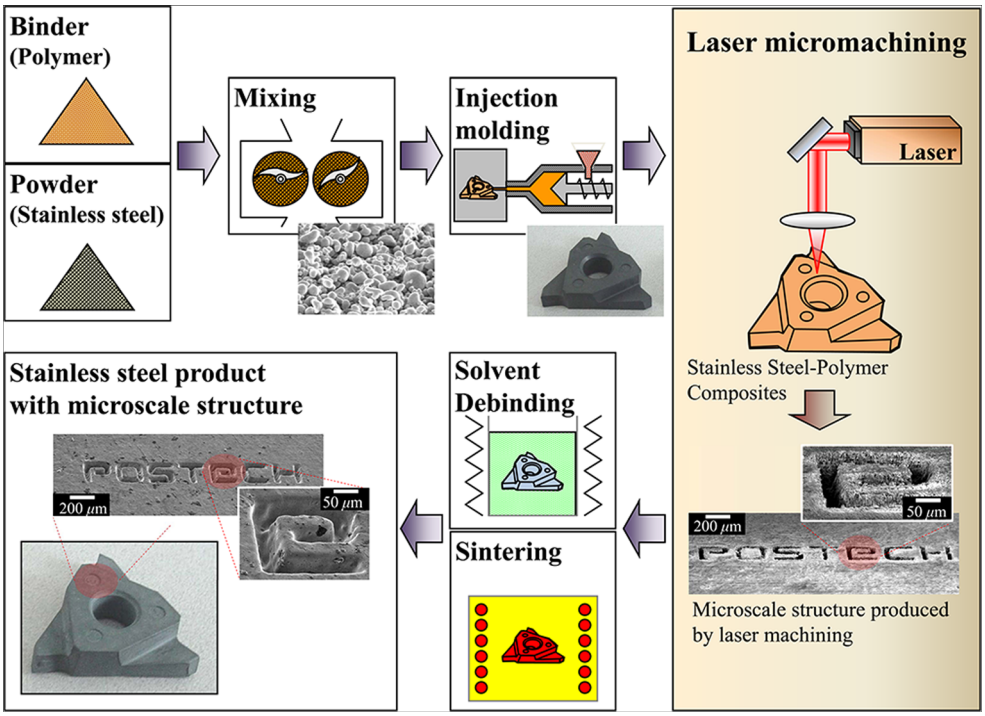

Fig. 1 Schematic diagram of the manufacturing process using laser micromachining applied to powder injection-molded parts, and examples of the fabricated microstructures

composites. The laser machining process was first used for via etching of ceramic–polymer composites using an ultraviolet (UV) excimer laser [17]. Several investigations have since examined the machining mechanisms to optimize the ceramic–polymer composite processing using a variety of laser sources, including a pulsed CO_2 laser [18], a Nd:YAG laser [19], and an excimer laser [20]. A gelcast alumina composite was subjected to Nd:YAG laser drilling, which is a highly effective approach to avoiding spattering and microcrack formation in the laser drilling of sintered ceramics [19]. A drilling process with a pulsed CO_2 laser was applied to alumina ceramic–polymer composite sheets, revealing that the etch rate varied depending on the spectral characteristics of the laser absorption cross-section for the polymer binder [18]. The weak absorption of the binder at the CO_2 laser wavelength causes the ceramic particles to heat significantly faster than the surrounding binder, which is then heated indirectly by heat diffusion from the particles [21, 22]. The polymer binder then decomposes, creating gas flows large enough to drag the freed ceramic particles away from the ablation site. In other words, a powder composite is machined by ablating a low-temperature polymer binder material. Similar mechanisms were proposed to explain the ablation of metal–polymer composites at relatively low laser fluences, i.e., below the ablation threshold of the metals, using a Nd:YAG laser beam [23]. The effects of the particle shape on the laser machining of a stainless steel–polymer composite were investigated, revealing that spherical-shaped particles are removed more effectively than irregularly shaped particles [24].

Despite the studies listed above, the mechanism by which powder composites (particularly the metal–polymer composites) are ablated under laser illumination, for various laser parameters, including wavelength, fluence, and pulse width, is not clearly understood. Previous studies mainly focused on relatively large-scale manufacturing processes, such as via hole drilling in ceramic–polymer composites, and only a small number of studies examined the micromachining characteristics. The interactions between ultrafast (sub-picosecond) UV laser pulses and powder composites have never been studied, although ultrafast UV beams are most suitable for micromachining of powder composites.

The main objective of this work is to analyze the interactions between nanosecond or femtosecond UV pulses and a stainless steel–polymer composite in an effort to identify optimal conditions for micromachining the composite material. Stainless steel was selected because it is one of the most common high-strength anti-corrosion materials used in industrial and scientific applications. Due to the physical properties of stainless steel, the material is not significantly ablated in the bulk state. The laser micromachining of stainless steel–polymer composites has been examined previously, revealing that the technique can achieve a feature width of 250 μm using ablation of a low-temperature polymer binder [23]; however, the study did not address the ablation characteristics under a range of incident laser fluences (e.g., above the ablation threshold of stainless steel). In this work, stainless steel–polymer composite samples consisting of a stainless steel powder (17-4PH) and a polymer binder (mixture of wax,

polypropylene, and polyethylene) were prepared. An excimer laser (wavelength λ=248 nm, full width at half maximum FWHM=25 ns) and, for the first time, a Ti:sapphire laser (λ=266 nm, FWHM=100 fs) were used to analyze the micromachining process over a wide range of parameters. Although femtosecond lasers are expected to perform better in the context of micromachining than nanosecond lasers, an excimer laser was tested to directly compare the results obtain with a ns laser with those with a fs laser. The material removal mechanisms were analyzed by varying the process parameters, including the laser fluence F and the pulse numbers N for the two laser sources. The effects of air jet blowing and liquid immersion on the micromachining performance were also examined. Microdrilling and grooving processes for forming circular/rectangular holes and microchannels were optimized and examined.

2 Theory

2.1 Interaction with the nanosecond UV laser

The stainless steel–polymer composite is inhomogeneous because it is a mixture of a polymer binder and a metal powder. Accordingly, spatial variations in the material properties complicated the interactions between the laser pulses and the material, which depends strongly on the wavelength, pulse width, laser fluence, etc. The nanosecond laser ablation of polymers generally occurs at a low laser fluence (range of 0.1 J/cm^2) relative to the laser ablation of metals [25]. The photochemical/photothermal dissociation of the polymer chain underlies the principle mechanism of polymer ablation via ns UV laser pulse, whereas laser ablation of bulk stainless steel mainly proceeds via a photothermal mechanism. Therefore, the ablation of stainless steel required a laser fluence approximately ten times larger than that required for polymers [26]. The mechanism underlying ns laser ablation of the stainless steel–polymer composite, therefore, depends critically on the incident laser fluence F (Fig. 2a). For F larger than the ablation threshold of the polymer binder ($F_{p,th}$) but smaller than the ablation threshold of stainless steel ($F_{s,th}$), decomposition of the polymer binder creates gas flow and removes the freed stainless steel particles from the surface [27]. On the other hand, for $F>F_{s,th}$, direct ablation of the stainless steel particles occurs with substantial agglomeration of the particles. At high laser fluences, the photothermal effect of a ns laser pulse can produce a molten polymer pool surrounding the stainless steel particles. In that case, the liquid surrounding accelerates melting of the stainless steel particles because the enhanced thermal transport. In the high-fluence regime, similar thermal mechanisms are expected to contribute to femtosecond laser ablation of the composite sample.

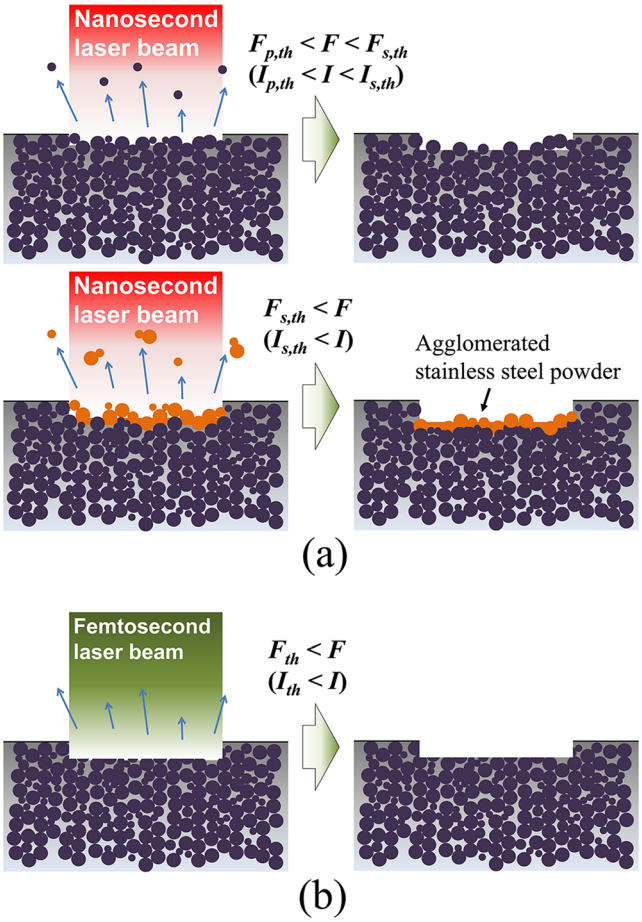

Fig. 2 Characteristics of the laser ablation of stainless steel–polymer composites using **a** nanosecond laser pulses and **b** femtosecond laser pulses

Rigorous simulations of the laser interactions with the powder composite are not easy, even for the case of a ns laser pulse. In this work, the thermal responses of the individual component materials to a single excimer laser pulse were calculated numerically. Absorption of the laser pulse by the target at time t=0 may be described as a one-dimensional temperature response $T(z,t)$ according to Fourier's law,

$$\rho C_p \frac{\partial T}{\partial t} - k\frac{\partial^2 T}{\partial z^2} = Q \tag{1}$$

where ρ is the density, C_p is the specific heat, k is the thermal conductivity, and z is the spatial coordinate. The source term Q represents the volumetric heat generation due to the laser beam absorption,

$$Q = (1-R)\alpha I_0 \exp(-\alpha z) F(t) \tag{2}$$

where R represents the reflectivity, α the absorption coefficient, and I_0 the irradiance (W/m^2) [28]. The

function $F(t)$ denotes the dimensionless temporal pulse shape expressed by

$$F(t) = \begin{cases} -\frac{1}{\tau_p}|t-\tau_p| + 1 & 0 < t < 2\tau_p \\ 0 & 2\tau_p < t \end{cases}, \quad (3)$$

where τ_p is the pulse width. All exterior boundary conditions were assumed to be adiabatic. The initial temperature over the calculation domain and the ambient temperature were assumed to be 25 °C. The material properties of polypropylene (PP), polyethylene (PE), wax, and stainless steel are listed in Table 1. The calculated peak temperatures of PP and PE were relatively low, as they absorbed the 248 nm UV radiation weakly (Fig. 3); however, these materials were ablated even at relatively low fluences due to incubation effects [29–31]. The experimentally measured ablation thresholds of PP and PE are 0.3 and 0.5 J/cm^2, respectively [32]. It is plausible that PP and PE decomposed due to the thermal energy absorbed by the stainless steel particles, the temperature of which increased to 490 °C (exceeding the decomposition temperature of PP and PE) at 0.35 J/cm^2. The peak temperature of wax, which comprised more than half of the binder, reached its decomposition threshold (200 °C) at F=0.4 J/cm^2 (Fig. 3). These results suggested that the decomposition of the binder system began at F=0.4 J/cm^2 by indirect heating of the binder. Accordingly, although direct photochemical ablation of the binder by a UV laser accelerates ablation of the composite, an IR laser can also ablate the composite by decomposing the binder photothermally. The temperature of stainless steel reached the melting point 1,400 °C at F=1 J/cm^2; therefore, melting of the stainless steel is expected for F>1 J/cm^2, consistent with the agglomeration properties depicted in Fig. 2a.

Table 1 Material properties of the polymer binder and stainless steel

	PP[a]	PE[b]	Wax[c]	Stainless steel[d]
Density (kg/m^3)	910	940	800	7,910
Specific heat (J/kgK)	1,700	2,250	2,900	503
Thermal conductivity (W/mK)	0.22	0.35	0.23	170
Absorption coefficient (m^{-1}, λ=248 nm)	$1\cdot10^4$	$1\cdot10^4$	$1.3\cdot10^5$	10^8
Reflectivity (λ=248 nm)	0.12	0.13	0.1	0.35
Melting temperature (°C)	170–297	140–203	49–71	1,400
Decomposition temperature (°C)	402–483	420–480	200	.

[a] References from [32, 40–43]

[b] References from [32, 42–44]

[c] References from [45–47]

[d] Reference from [48]

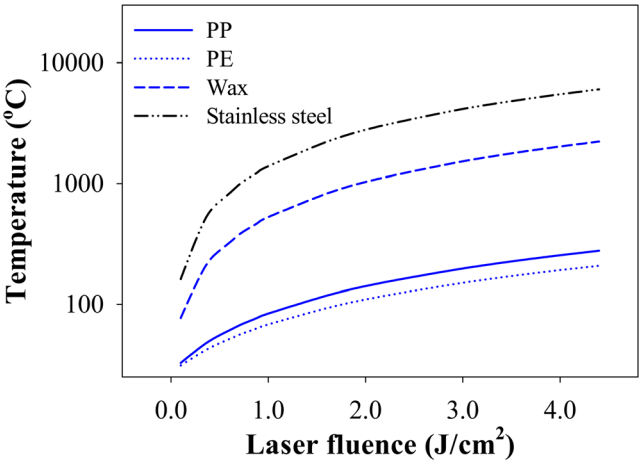

Fig. 3 Calculated temperature responses to a ns laser pulse in air

2.2 Interactions with the femtosecond UV laser

The fs laser pulse during fs laser ablation excites valence electrons into the conduction band via photoionization and avalanche ionization. The excited free electrons further absorb laser energy and transfer the energy to ions, thereby increasing the sample temperature. A high-intensity fs laser pulse can ablate materials regardless of their optical properties via thermal and/or nonthermal (e.g., Coulomb explosion) mechanisms [33]. Although the UV wavelength (266 nm) of the fs laser is absorbed by the binder as well as by the stainless steel particles, nonlinear absorption mechanisms, such as multiphoton absorption, also contribute to ablation of the polymer binder. Accordingly, the fs laser ablation threshold of the binder is determined by complicated mechanisms and different from that of stainless steel. Theoretical predictions of the interactions between a fs laser pulse and a polymer resin or stainless steel are not straightforward because they are mixtures and relatively little information is available regarding the electronic structures and phonon–electron coupling. Previous experimental studies showed that 150 fs laser pulses with F>0.1 J/cm^2 (threshold irradiance I_{th}~1 TW/cm^2) could ablate common polymers and bulk stainless steel (304) [34, 35]. In the case of PE, the fs laser ablation threshold is 0.06 J/cm^2 [35]. The power density of the fs laser beam employed in the present work was on the order of 1 TW/cm^2, whereas that of the ns laser beam was on the order of 1 GW/cm^2. Accordingly, direct ablation of both the polymer resin and the stainless steel particles was possible with low thermal effects (Fig. 2b). In other words, the stainless steel–polymer composite was expected to behave as a homogeneous sample composed of a single material during fs laser ablation.

Table 2 Particle size distribution in the stainless steel powder

Particle size	D_{10}	D_{50}	D_{90}	Mean
(μm)	3.09	7.63	15.8	8.88

3 Experimental

A stainless steel–polymer composite sample was prepared by a powder injection molding process using an injection molding machine (Sodick Plustech TR30EH). The sample consisted of spherical stainless steel particles (17-4PH, water-atomized, ATMIX) and a polymer binder with a volume ratio of 6:4. The ratio (60 % solids loading) was selected to minimize shrinkage of the sintered parts while maintaining the fluidity required for injection molding of the stainless steel particles. Solids loading values in the range 45–63 % are commonly used for injection molding of stainless steel particles [13]. The polymer binder was composed of 57 % wax, 25 % polypropylene (PP), 15 % polyethylene (PE), and 3 % stearic acid (SA). The cumulative size distribution of the stainless steel particles was measured using a particle size analyzer (Horiba LA-950), as summarized in Table 2. D_{50}=7.6 μm means that 50 % of the particles in the sample were larger than 7.6 μm, and 50 % were smaller than 7.6 μm.

A KrF excimer laser (λ=248 nm, FWHM=25 ns) and a Ti:sapphire femtosecond laser with a regenerative amplifier and a third harmonic generator (λ=266 nm, FWHM=100 fs, M-squared factor M^2<1.3) were used in the experiment. The experimental setup included laser sources, a beam delivery and monitoring system, and a micropositioning stage (Fig. 4). A mask projection micromachining system with a demagnification ratio of 10 was used in the excimer laser experiment. On the other hand, the samples were processed at the focal position in the Ti:sapphire laser experiment. Anti-reflective lenses with focal lengths of 10 and 5 cm were used to focus the excimer and Ti:sapphire beams, respectively. Aluminum masks with square apertures or circular apertures (0.5–1 mm) were used for the excimer laser experiment. In the Ti:sapphire laser experiment, a 1-mm circular aperture was used to reduce the output beam energy to a range appropriate for direct-writing laser machining applications. A 100 μm-sized square spot and a 50 μm-sized circular spot in the case of the excimer laser and a circular spot 20 μm in diameter (calculated theoretically) in the case of the Ti:sapphire laser were generated. The pulse energy E of the excimer laser was varied over the range 70–280 μJ (F=0.7–2.8 J/cm^2). E for the Ti:sapphire laser was varied over the range 0.2–3.5 μJ (F=0.06–1.1 J/cm^2) using a half wave plate and a polarizer. The sample position was controlled using a three-dimensional translation stage with a resolution of 1 μm.

To analyze the effects of air jet blowing on the process performance, an air jet injection system with an impingement angle of 45° was constructed using a 500 μm diameter nozzle and a pressure regulator (3 bar). The distance between the nozzle tip and the specimen was maintained at 3 mm. The effects of the ambient liquid were examined by submerging the sample in deionized (DI) water to a depth of about 1 mm. After laser processing, the surface was analyzed using an optical microscope and a scanning electron microscope (SEM). The topography of the laser-processed spot was quantified using a 3D surface profiler.

4 Results and discussion

4.1 Nanosecond UV laser processing

The behaviors of the stainless steel particles at different laser fluences were inspected by SEM imaging of the ablated sample (Fig. 5). At F=0.7 J/cm^2, only the polymer binder

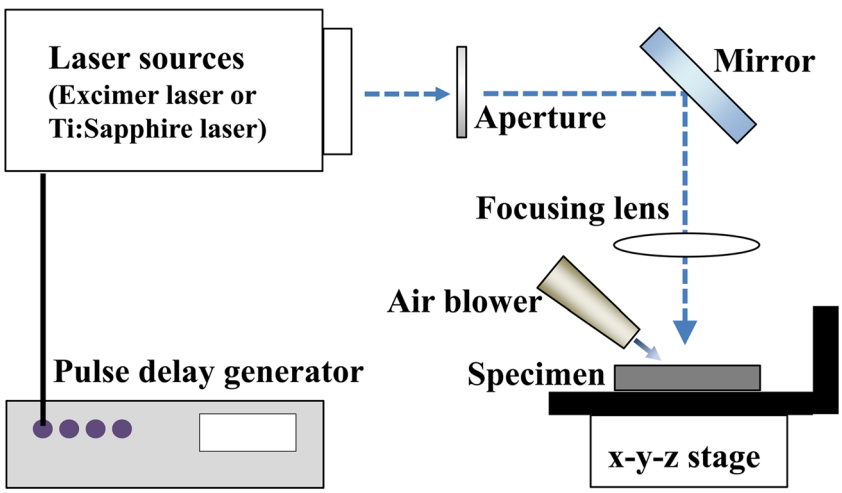

Fig. 4 Experimental setup used for laser micromachining

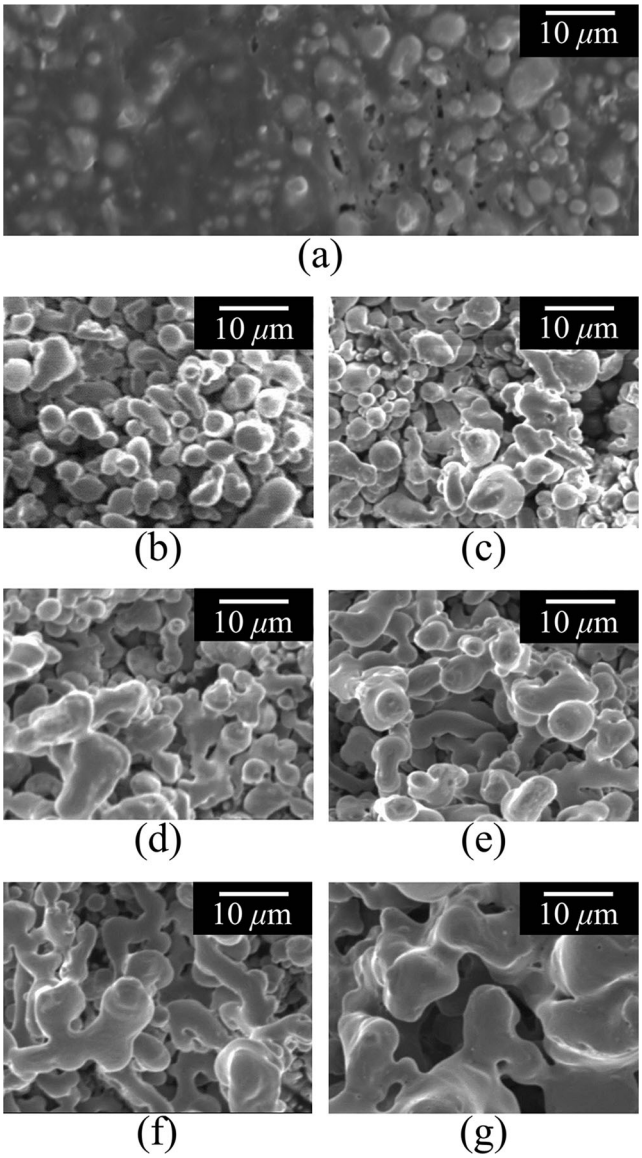

Fig. 5 SEM images showing **a** the bare stainless steel–polymer composite and the agglomeration characteristics of the stainless steel particles, corresponding to laser fluences of b 0.7 J/cm^2, **c** 1.1 J/cm^2, **d** 1.6 J/cm^2, **e** 2.1 J/cm^2, **f** 2.4 J/cm^2, and **g** 2.8 J/cm^2

was removed, leaving separate stainless steel particles that showed low thermal effects, as shown in Fig. 5b. As F increased beyond 1 J/cm^2, melting and aggregation of the stainless steel particles generated resolidified aggregates (Fig. 5c–g). The stainless steel particles with an initial mean size of 8.9 μm finally formed an agglomerated particle network with an average cluster size of 100 μm (Fig. 5g). Figures 3 and 5b clarified that the mechanism underlying material removal was dominated by polymer binder dissociation in the low-fluence regime (<1 J/cm^2). This mechanism is similar to that of pulsed laser ablation at infrared and visible wavelengths [18, 19, 21, 22]. In the high-fluence regime (>1 J/cm^2), on the other hand, the mechanism underlying direct ablation of the stainless steel particles remained undetermined, although the formation of large agglomerates blocked the laser beam and reduced the ablation rate. These results are in good agreement with the numerical calculations shown in Fig. 3 and the ablation mechanisms depicted in Fig. 2a. Melting of the stainless steel occurred at ~1 J/cm^2 both in the numerical calculation and in the experiment. The ablation process was significantly affected by the air jet blowing and the ambient environment. In the air, laser irradiation at 1 J/cm^2 without the external air jet could not effectively remove the stainless steel particles from the ablation surface because polymer ablation alone did not provide particles with sufficient detachment forces (Fig. 6a). On the other hand, laser irradiation at the same fluence in the presence of an external airflow substantially increased the uniform ablation of the sample (Fig. 6b). A process, that is, laser ablation in DI water, significantly increased the ablation rate and reduced thermal side effects (Fig. 6c), as in typical liquid-phase laser ablation processes; however, immersion generated irregular surface profiles. Ablation was enhanced to a larger degree by the liquid immersion than by the blowing of an air jet. The enhanced ablation and non-uniformity appeared to arise from the photomechanical effects of the confined plasma and liquid cavitation [36, 37]. In the case of fs laser ablation, because the ablation enhancement by plasma confinement and the thermal side effects are relatively weak, laser ablation in DI water was not tested. Consequently, all experiments, including those performed using the fs laser, were therefore conducted under an air jet.

The ablation depth of the stainless steel–polymer composite increased linearly with the pulse number N at laser fluences lower than ~2 J/cm^2, although it eventually saturated at $F \approx 2.5$ J/cm^2 due to blocking of the incident laser pulse by

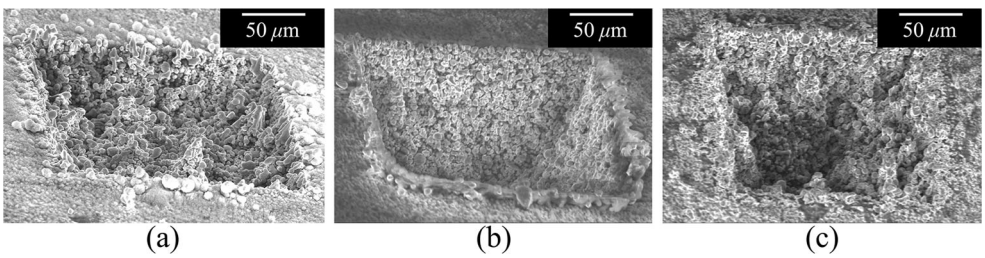

Fig. 6 Stainless steel–polymer composite ablated using 5,000 pulses of a ns laser with **a** no environmental control, **b** air jet blowing, or **c** a water film (F=1 J/cm^2)

the agglomerated stainless steel (Fig. 7a). The ablation rate of the stainless steel–polymer composite was measured as a function of the laser fluence (Fig. 7b). The ablation rate, that is, the ablation depth per pulse, was obtained by measuring the average ablation depth after 5,000 pulses. Figure 7b presents the reported ablation rates of some component materials (PP, PE, and bulk stainless steel) for reference purposes. The measured ablation threshold during ns laser processing was F=0.5 J/cm^2 (Fig. 7b). The threshold was substantially lower than that of bulk stainless steel and was the same order of magnitude as that of the polymers. This indicated that the ablation of the stainless steel–polymer composite occurred via ablation of the polymer binder. The measured ablation threshold also agreed well with the numerical predictions described in Section 2.1. The ablation rate of the stainless steel–polymer composite was substantially lower than the rates of PE and PP (0.1–5 μm/pulse) but much higher than the rate for bulk stainless steel (10 nm/pulse), possibly because the stainless steel particles were exposed to the surface, melted, and agglomerated at high F, thereby blocking the laser beam. The slope of the ablation rate curve decreased significantly as F exceeded 2 J/cm^2.

Microholes and channels were fabricated using an excimer laser, as shown in Fig. 8. A series of 100 μm square holes and 50 μm circular holes were obtained by percussion drilling with N=20,000 at 1.6 J/cm^2 (Fig. 8a, b). The depth of the drilled holes was 500 μm in both cases. Accordingly, the aspect ratio of the structures 50 μm holes was 10. Microchannels 100 and 50 μm in width were also fabricated by translating the sample at a speed of 10 μm/s at F=1.6 J/cm^2 (Fig. 8c, d) and, from the cross-section images, which have 600 and 550 μm machining depth, respectively. During the process, the laser pulse scanned the sample 200 times at 10 Hz, resulting in N=20,000. Considering that the resolution of conventional μ-PIM processes using stainless steel powder (17-4PH, D_{50}=9.6 μm) is 160 μm [38], these results clearly showed that the UV laser-based microstructuring process, even using a ns laser, has strong potential as a micromanufacturing tool for stainless steel–polymer composites.

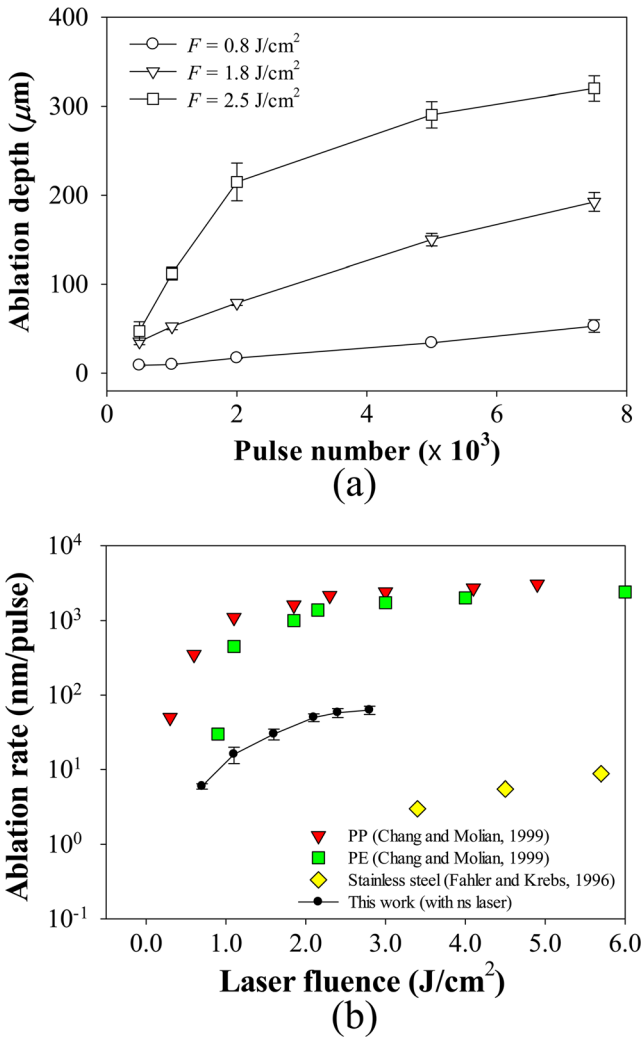

Fig. 7 **a** Ablation depth as a function of pulse number, and **b** comparison of the ablation rates of bulk PP, PE [32], and stainless steel [26] under 248 nm ns laser irradiation with air jet blowing

4.2 Femtosecond UV laser processing

The peak power of a fs laser pulse is much higher than that of a ns laser pulse [39]. As expected, the ablation depth was linearly proportional to N, and the ablation rate based on N=5,000 laser pulses (Fig. 9) was much greater than that obtained using the excimer laser (Fig. 7). In both the ns and fs laser cases, the ablation rates measured for the stainless

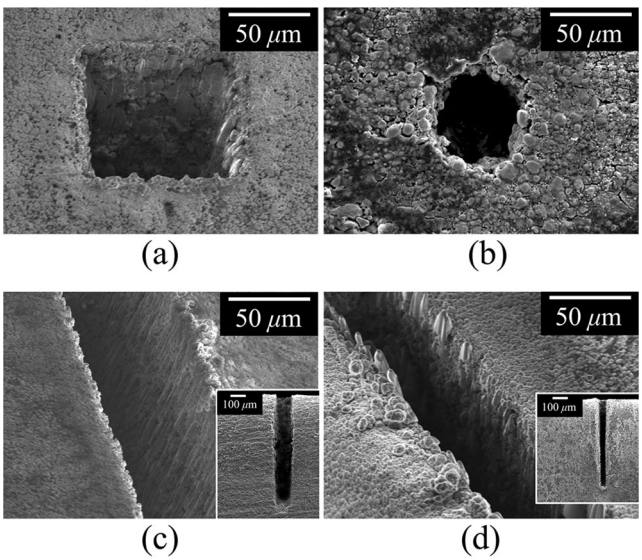

Fig. 8 Machining results (drilling and channeling) using ns laser pulses. **a** a square hole 100 μm in length and **b** a circular hole 50 μm in diameter, prepared using 20,000 pulses of the laser; **c** microchannels 100 μm wide or **d** 50 μm wide (F=1.6 J/cm^2)

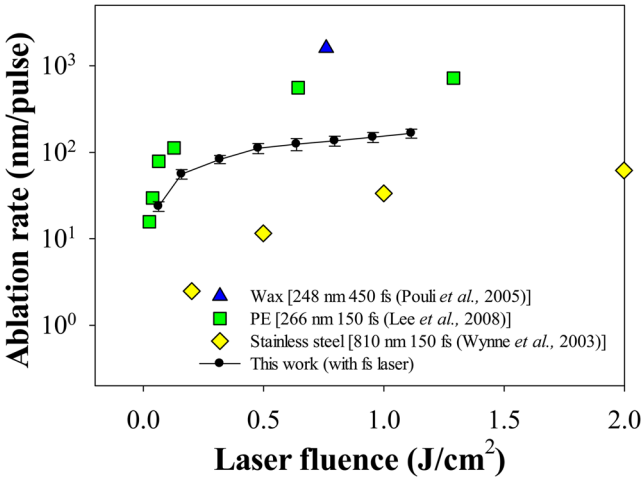

Fig. 9 Comparison of the ablation rates of bulk wax [47], PE [34], and stainless steel by using fs laser irradiation

steel–polymer composite were much higher than the rates for bulk stainless steel. SEM images of a sample ablated by fs laser pulses showed no signs of melting or agglomeration of the particles (Fig. 10), in contrast with samples ablated using a ns laser (Fig. 5). Microstructure fabrication was demonstrated using fs laser pulses (Fig. 11). Circular microholes were drilled using the percussion process with N=10,000 at F=0.06 and 0.16 J/cm^2. The results demonstrated the fabrication of 15 μm holes with depths up to 150 μm (Fig. 11a) and 20 μm holes with depths up to 400 μm (Fig. 11b). Microchannel fabrication was demonstrated by translating the sample at a speed of 10 μm/s. In the process, the laser pulse scanned the sample 40 times at 1 kHz, resulting in N=80,000 pulses. Microchannels of different sizes, including 25 μm in width and 300 μm in depth (Fig. 11c) and 28 μm in width and 400 μm in depth (Fig. 11d), were successfully fabricated. The resolution of the fs laser micromachining process, which is generally determined by the spot size, the

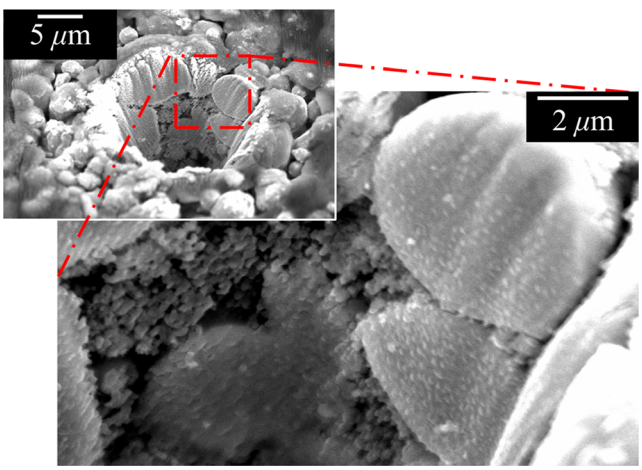

Fig. 10 Powder shapes at the ablation sites using fs laser pulses (F=0.32 J/cm^2)

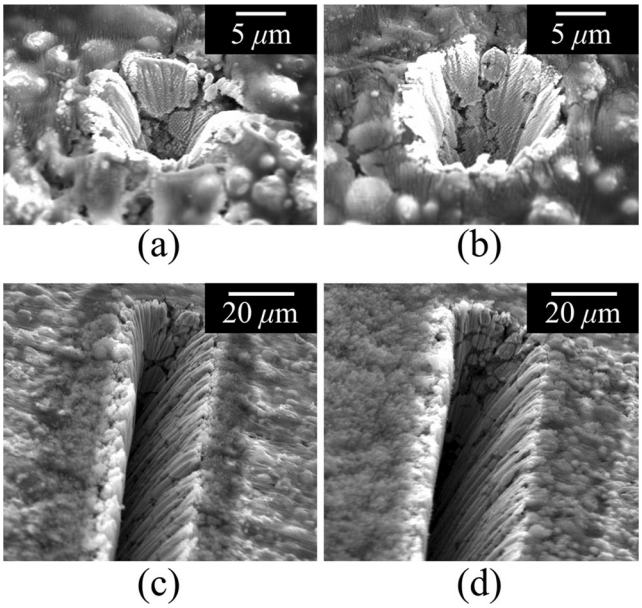

Fig. 11 Micromachining results using fs laser pulses. Percussion laser machining with 10,000 pulses of peak laser energy **a** 0.2 μJ (0.06 J/cm^2) and **b** 0.5 μJ (0.16 J/cm^2); channeling at a peak laser energy of **c** 1.0 μJ (0.32 J/cm^2) and **d** 2.0 μJ (0.64 J/cm^2)

thermal effects, and the resolution of the translation stage, can be smaller than the size (mean, 8.8 μm) of the embedded particles. Consequently, the resolution of the micromachining process described here was about 10 μm. These results suggest that fs laser processing of stainless steel–polymer composite provides a micromachining processes with good resolution, regardless of the size distribution of the stainless steel particles, in contrast with conventional μ-PIM processes.

5 Conclusions

In this work, we investigated the micromachining of a stainless steel–polymer composite using ns and fs UV lasers. The ablation mechanism varied significantly depending on the laser pulse width and fluence. Nanosecond laser ablation occurred largely via the removal of embedded stainless steel particles because the polymer resin thermally decomposed. On the other hand, the fs laser pulse directly ablated, that is, cut, the particles, thereby increasing the spatial resolution of the ablation process. An air jet increased the ablation rate and smoothed the surface during ns laser processing. Liquid immersion during ablation enhanced the ablation rate but increased the surface roughness. Micromachining using ns and fs UV lasers was demonstrated by fabricating high-aspect-ratio microstructures with spatial resolutions of 50 and 10 μm, respectively.

Acknowledgments This work was supported by the National Research Foundation of Korea (NRF) grant funded by the Korea government (MSIP) (No. 2010-0017848, No. 2011-0030075).

References

1. German RM (1993) Powder Metall Int 25:165
2. Loh NH, Tor SB, Khor KA (2001) J Mater Process Tech 108:398
3. Liu ZY, Loh NH, Tor SB, Khor KA, Murakoshi Y, Maeda R, Shimizu T (2002) J Mater Process Tech 127:165
4. Cai LX, German RM (1995) Int J Powder Metall 31:257
5. Fu G, Tor S, Loh N, Tay B, Hardt DE (2007) J Micromech Microeng 17:1803
6. Tay B, Loh NH, Tor SB, Ng FL, Fu G, Lu XH (2009) Powder Technol 188:179
7. Zauner R (2006) Microelectron Eng 83:1442
8. Hsu KC, Lin CC, Lo GM (1994) Powder Metall 37:272
9. Barreiros FM, Vieira MT (2006) Ceram Int 32:297
10. Zhu BJ, Qu XH, Tao Y, Xiao PG, Qin ML (2002) Rare Metal Mat Eng 31:232
11. Urval R, Lee S, Atre SV, Park SJ, German RM (2010) Powder Metall 53:71
12. Yu PC, Li QF, Fuh JYH, Li T, Ho PW (2009) Microsyst Technol 15:401
13. Ahn S, Park SJ, Lee S, Atre SV, German RM (2009) Powder Technol 193:162
14. Meng JH, Loh NH, Fu G, Tor SB, Tay BY (2010) J Alloy Compd 496:293
15. Liu L, Loh NH, Tay BY, Tor SB (2011) Powder Technol 206:246
16. Piotter V, Plewa K, Mueller T, Ruh A, Vorster E, Ritzhaupt-Kleissl HJ, Hausselt J (2010) Key Eng Mat 447–448:351
17. Anon, IBM technical disclosure bulletin 28, 1216 (1985).
18. Imen K, Allen SD (1999) IEEE Trans Adv Pack 22:620
19. Guo D, Cai K, Huang Y, Li LT (2003) Appl Phys Mater 76:1121
20. Chen J, Yue C, Zhang Y, Wang X, Zuo T (2004) Proc SPIE - Intl Soc Opt Eng 5641:205
21. Sola D, Gurauskis J, Pena JI, Orera VM (2009) Mater Res Bull 44:1910
22. Nowak K, Baker H, Hall D (2011) Appl Phys Mater 103:1033
23. Slocombe A, Li L (2000) Appl Surf Sci 154:617
24. Slocombe A, Taufik A, Li L (2000) Appl Surf Sci 168:17
25. Knowles MRH, Rutterford G, Karnakis D, Ferguson A (2007) Int J Adv Manuf Tech 33:95
26. Fahler S, Krebs HU (1996) Appl Surf Sci 96–8:61
27. Nowak KM, Baker HJ, Hall DR (2006) Appl Phys Mater 84:267
28. Bäuerle D (2000) Laser processing and chemistry, 3rd edn. Springer, Berlin
29. Küper S, Stuke M (1987) Appl Phys B Photophys Laser Chem 44: 199
30. Srinivasan R, Braren B, Casey KG (1990) J Appl Phys 68:1842
31. Sutcliffe E, Srinivasan R (1986) J Appl Phys 60:3315
32. Chang T-C, Molian PA (1999) J Manuf Proc 1:1
33. Stoian R, Rosenfeld A, Ashkenasi D, Hertel IV, Bulgakova NM, Campbell EEB (2002) Phys Rev Lett 88:976031
34. Lee AJ, Dawes JM, Withford MJ (2008) J Laser Appl 20:154
35. Wynne AE, Stuart BC (2003) Appl Phys Mater 76:373
36. Zhu S, Lu YF, Hong MH (2001) Appl Phys Lett 79:1396
37. Kang HW, Lee H, Welch AJ (2008) J Appl Phys 103:083101
38. Okubo K, Tanaka S, Ito H (2010) Microsyst Technol 16:2037
39. Weck A, Crawford THR, Wilkinson DS, Haugen HK, Preston JS (2008) Appl Phys Mater 90:537
40. Kawanishi S, Shimizu Y, Sugimoto S, Suzuki N (1991) Polymer 32: 979
41. Aboulkas A, El Harfi K, El Bouadili A, Chanâa M, Mokhlisse A (2007) J Therm Anal Calorim 89:203
42. Lide DR (2003) Handbook of chemistry and physics, 84th edn. CRC Press, Boca Raton
43. Philipp HR, Cole HS, Liu YS, Sitnik TA (1986) Appl Phys Lett 48: 192
44. Cho JW, Woo KS, Chun BC, Park JS (2001) Eur Polym J 37:1227
45. Grant RH, Heisler GM, Gao W, Jenks M (2003) Agr Forest Meteorol 120:127
46. Hirschausen D, Kane DM (2002) J Appl Phys 92:4201
47. Pouli P, Melessanaki K, Giakoumaki A, Argyropoulos V, Anglos D (2005) Spectrochim Acta B 60:1163
48. Jyumonji M, Sugioka K, Takai H, Tashiro H, Toyoda K (1995) Appl Phys Mater 60:41